

Anti-topological crystal and non-Abelian liquid in twisted semiconductor bilayers

Aidan P. Reddy,^{1,*} D. N. Sheng,^{2,†} Ahmed Abouelkomsan,^{1,‡} Emil J. Bergholtz,^{3,§} and Liang Fu^{1,¶}

¹*Department of Physics, Massachusetts Institute of Technology, Cambridge, Massachusetts 02139, USA*

²*Department of Physics and Astronomy, California State University Northridge, Northridge, California 91330, USA*

³*Department of Physics, Stockholm University, AlbaNova University Center, 106 91 Stockholm, Sweden*

(Dated: December 2, 2024)

We show that electron crystals compete closely with non-Abelian fractional Chern insulators in the half-full second moiré band of twisted bilayer MoTe₂. Depending on the twist angle and microscopic model, these crystals can have non-zero or zero Chern numbers. The latter relies on cancellation between contributions from the full first miniband (+1) and the half-full second miniband (-1). For this reason, we call it an *anti-topological crystal*. Surprisingly, it occurs despite the lowest two non-interacting bands in a given valley having the same Chern number of +1. The anti-topological crystal is a novel type of electron crystal that may appear in systems with multiple Chern bands at filling factors $n > 1$.

Introduction– Moiré superlattices made of twisted semiconductor bilayers host a variety of topological and symmetry-broken electronic phases. In twisted MoTe₂ (t MoTe₂), spatially varying intralayer potential and interlayer tunneling together produce topological minibands [1, 2]. At partial filling of the lowest band $n < 1$, Coulomb interactions give rise to Ising ferromagnets [3, 4], fractional quantum anomalous Hall (FQAH) states [2, 3, 5–12], and anomalous composite Fermi liquids [9, 13, 14], and other remarkable phenomena [15–17].

Even more intriguingly, recent theoretical works have proposed a non-Abelian fractional Chern insulator (FCI) at half-filling of the *second* moiré band in t MoTe₂ [18–22], which corresponds to $n = 3/2$ or $5/2$ depending on the degree of spin polarization. This state arises from a close resemblance between the wavefunctions of the second miniband and those of the first-excited Landau level (1LL), which hosts a non-Abelian state at $n = 5/2$ [23–26]. However, these studies have not systematically studied the stability of the non-Abelian FCI, or the possibility of competing states in t MoTe₂ at $n > 1$.

It is natural to expect that the proposed non-Abelian FCI competes closely with other phases including electron crystals [27]. For instance, in the 1LL, a slight deviation of the two-body interaction from $1/r$ can replace the non-Abelian state with a composite Fermi liquid or a stripe charge density wave [28]. The competition between topology and crystalization also occurs in the lowest band of t MoTe₂: while the FQAH state appears robustly at $n = \frac{2}{3}$, a generalized Wigner crystal with zero Hall conductance is predicted and observed at $n = \frac{1}{3}$ [7, 11, 15].

In this work, we study the phase diagram of t MoTe₂ at half-filling of the second miniband. We identify commensurate electron crystals with unit cells quadrupled relative to the moiré unit cell. We work with both the adiabatic model [29–31], previously shown to host a non-Abelian FCI phase [18], and the lowest-harmonic continuum model from which the adiabatic model is derived [1]. The lowest two non-interacting minibands in a fixed valley of both models have the same Chern number +1

throughout the twist angle range we focus on. Yet remarkably, they both host “anti-topological” crystals with vanishing many-body Chern numbers $C = 0$. Further, we find that, in the adiabatic model, two additional crystal phases with $C = 2$ and 1 appear at angles nearby that at which a $C = \frac{3}{2}$ non-Abelian FCI appears.

We base our conclusions on a combination of band-projected exact diagonalization and all-band Hartree-Fock calculations. The anti-topological crystal we study here at $n = 3/2$ shares a quadrupled unit cell in common with the QAH crystal recently proposed at $n = 1/2$ in t MoTe₂ but differs in its Chern number [32]. Our work identifies the anti-topological crystal as a new type of electron crystal distinct from crystals in partially occupied Chern bands studied previously, and establishes it as the competing state to the non-Abelian FCI state at half filling of the second miniband in t MoTe₂.

Recent experiments report the appearance of a $C = 2$ Chern insulator under a finite magnetic field stemming from $n = 2$, providing evidence that the first and second moiré bands in a given valley have the same Chern number [33]. Meanwhile, an insulating state appears near $n = \frac{3}{2}$ at finite magnetic field. Our theory suggests a possible explanation of the $n = \frac{3}{2}$ insulating state as an anti-topological crystal.

Incompressible liquids and crystals in adiabatic model– We begin by studying the “adiabatic” model for t MoTe₂ [18, 29], whose one-body spin/valley projected Hamiltonian takes the form

$$H = \frac{(\mathbf{p} + \frac{e}{c}\mathbf{A}(\mathbf{r}))^2}{2m} + V(\mathbf{r}). \quad (1)$$

Here, $\mathbf{A}(\mathbf{r})$ is a vector potential whose corresponding magnetic field $\mathbf{B}(\mathbf{r}) = \nabla \times \mathbf{A}(\mathbf{r})$ varies with moiré periodicity and averages to one flux quantum per unit cell. In brief, this model follows from taking the lowest-harmonic continuum model introduced in Ref. [1] and constraining holes’ layer pseudospin to align with the effective layer “Zeeman” field $\mathbf{J}(\mathbf{r})$ whose z component corresponds to interlayer potential and xy components correspond to in-

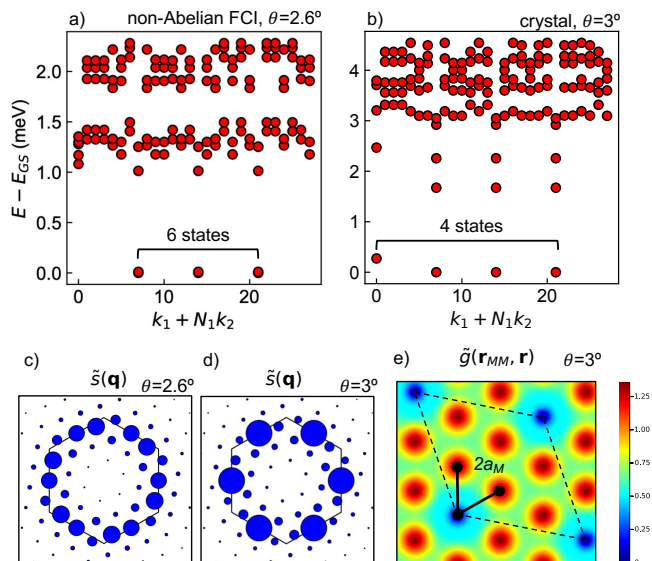


FIG. 1. **Non-Abelian FCI and electron crystal phases in the adiabatic model.** Representative energy spectra within (a) the non-Abelian FCI and (b) crystal phases, at $\theta = 2.6^\circ$ and 3° respectively. Modified structure factor at (c) $\theta = 2.6^\circ$ and (d) $\theta = 3^\circ$. The first moiré Brillouin zone is outlined, the radius of the marker is proportional to $\tilde{s}(\mathbf{q})$, $\tilde{s}(0) = N$ is omitted, and the maxima of $\tilde{s}(\mathbf{q})$ at 2.6° and 3° are 0.472 and 0.721 respectively. (e) Modified pair correlation function at $\theta = 3^\circ$. A single supercell is outlined. $\epsilon = 5$ and cluster 28 are used [34].

terlayer tunneling. Throughout this work, we use the continuum model parameters for $t\text{MoTe}_2$ reported in Ref. [11]. We focus on filling of $n = \frac{3}{2}$ of a hole per moiré unit cell and assume full spin (or, equivalently, valley) polarization. An external magnetic field may drive full spin polarization through the Zeeman effect when it does not occur spontaneously. In our exact diagonalization calculations, we make a variational approximation by assuming that the lowest spin- \uparrow miniband is full and constraining the remaining holes to the second spin- \uparrow miniband. Though inert, the holes in the full lowest band add a Hartree-Fock self-energy $\Sigma(\mathbf{k})$ to the second band's one-body dispersion [18].

In Figs. 1(a,b), we contrast an example many-body spectrum at $n = \frac{3}{2}$ and an interlayer twist angle of $\theta = 2.6^\circ$ with one at 3° . The first exhibits a sixfold ground state quasidegeneracy as expected of an FCI state with Pfaffian or anti-Pfaffian topological order and even fermion number [35], while the second exhibits a fourfold ground state quasidegeneracy. The center-of-mass crystal momenta of the four ground states at 3° differ by reciprocal lattice vectors of a 2×2 enlarged unit cell (m points, or midpoints of the moiré Brillouin zone edges), indicating spontaneous translation symmetry breaking.

To further probe crystallization at $\theta = 3^\circ$, we study density correlation functions. We find that the

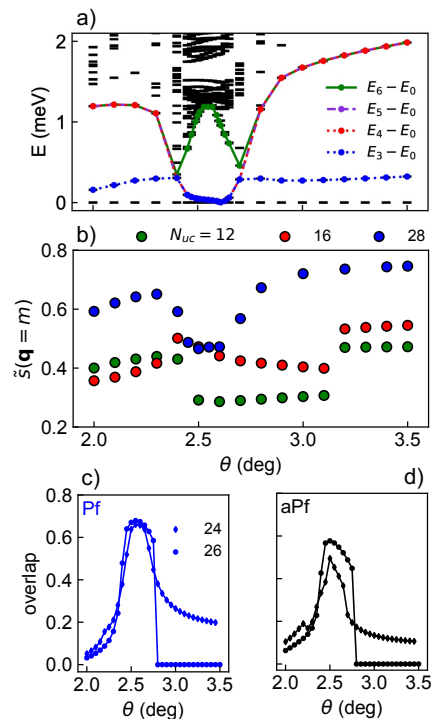


FIG. 2. **Phase diagram of adiabatic model.** (a) Low-lying energy spectrum on cluster 28 as a function of twist angle θ . (b) Modified structure factor evaluated at $\mathbf{q} = m$ as a function of twist angle θ . Overlap of ground state with the Pfaffian (c) and anti-Pfaffian (d) model wavefunctions as a function of θ on clusters 24 and 26 [34]. $\epsilon = 5$ is used.

1LL-like character of the second miniband's wavefunctions suppresses density fluctuations at $\mathbf{q} = m$ and, therefore, masks signatures of crystallization in conventional density correlation functions at finite size. This is a consequence of a zero in the projection of the density operator $e^{i\mathbf{q}\cdot\mathbf{r}}$ to the 1LL at $|\mathbf{q}| \approx |m|$ and is familiar from studies of higher Landau levels [28, 34, 36, 37]. To expose translation symmetry breaking, we define “modified” correlation functions by replacing the the projected density operator of the second band, $\tilde{\rho}(\mathbf{q}) = \sum_{\mathbf{k}} \langle u_{2,\mathbf{k}-\mathbf{q}} | u_{2,\mathbf{k}} \rangle c_{2,\mathbf{k}-\mathbf{q}}^\dagger c_{2,\mathbf{k}}$, with $\tilde{\rho}(\mathbf{q}) = \sum_{\mathbf{k}} \langle u_{\text{LLL},\mathbf{k}-\mathbf{q}} | u_{\text{LLL},\mathbf{k}} \rangle c_{2,\mathbf{k}-\mathbf{q}}^\dagger c_{2,\mathbf{k}}$ where $\langle u_{\text{LLL},\mathbf{k}-\mathbf{q}} | u_{\text{LLL},\mathbf{k}} \rangle = e^{\ell^2(i\mathbf{q}\wedge\mathbf{k}/2 - \mathbf{q}^2/4)}$. Similarly, we define $\tilde{n}(\mathbf{r}) = \sum_{\mathbf{k},\mathbf{k}'} \psi_{\text{LLL},\mathbf{k}'}^*(\mathbf{r}) \psi_{\text{LLL},\mathbf{k}}(\mathbf{r}) c_{2,\mathbf{k}'}^\dagger c_{2,\mathbf{k}}$. With these replacements, we define a “modified” projected structure factor

$$\tilde{s}(\mathbf{q}) = \frac{1}{N} \langle \tilde{\rho}(-\mathbf{q}) \tilde{\rho}(\mathbf{q}) \rangle \quad (2)$$

and modified pair correlation function

$$\tilde{g}(\mathbf{r}', \mathbf{r}) = \frac{\langle \tilde{n}(\mathbf{r}) \tilde{n}(\mathbf{r}') - \delta(\mathbf{r}, \mathbf{r}') \tilde{n}(\mathbf{r}) \rangle}{\langle \tilde{n}(\mathbf{r}') \rangle \langle \tilde{n}(\mathbf{r}) \rangle} \quad (3)$$

where N is the number of holes in the second miniband and $\langle \rangle$ the expectation value with respect to all

degenerate ground states. We fix our gauge such that $\langle \psi_{1LL,\mathbf{k}} | \psi_{2,\mathbf{k}} \rangle$ is real and positive. Here, $|\psi_{2,\mathbf{k}}\rangle$ and $|\psi_{1LL,\mathbf{k}}\rangle$ are magnetic Bloch states in the second miniband of the adiabatic model and the 1LL respectively.

In the putative crystal phase at 3° , $\tilde{s}(\mathbf{q})$ shows incipient Bragg peaks at the m points of the moiré Brillouin zone (Fig. 1 (a)). This is consistent with spontaneous quadrupling of the moiré unit cell. In contrast, in the FCI state at 2.6° , $\tilde{s}(\mathbf{q})$ is nearly isotropic as shown in Fig. 1(c). The modified pair correlation function $\tilde{g}(\mathbf{r}', \mathbf{r})$ shown in Fig. 1(c) also evidences the crystal's 2×2 symmetry-breaking pattern. At smaller angles such as $\theta = 2.3^\circ$, we find behavior in the many-body spectrum and projected structure factor similar to 3° [34].

Having established a crystal phase, we now study the phase diagram's dependence on interlayer twist. In Fig. 2(a), we plot the many-body spectrum as a function of θ . We find three distinct regions of 4-, 6-, and 4-fold ground state quasidegeneracy that correspond to crystal, FCI, and crystal phases respectively. In Fig. 2(b), we show $\tilde{s}(\mathbf{q} = m)$ as a function of twist angle. Within the FCI phase ($\theta \sim 2.6^\circ$), $\tilde{s}(m)$ is smaller than at other twist angles and $\tilde{s}(\mathbf{q})$ is nearly isotropic (Fig. 1(c)). Within the crystal phase $\theta \gtrsim 2.7^\circ$, $\tilde{s}(m)$ is large and grows with system size, consistent with long-range order in the thermodynamic limit. For $\theta \lesssim 2.4^\circ$, $\tilde{s}(m)$ also grows with system size (save for the smallest system studied).

We further characterize the evolution of the quantum ground state by calculating its overlaps with model non-Abelian FCI states. Fig. 2(c) shows that the overlap between the Coulomb ground state and exact model Pfaffian and anti-Pfaffian states become large in a twist angle window similar to that in which the 6-fold ground state quasidegeneracy appears (Fig. 1(a)) [18]. The Pfaffian overlap consistently exceeds the anti-Pfaffian overlap, suggesting that the former is more likely to emerge in the thermodynamic limit, in agreement with the conclusions of Ref. [18] based on overlaps at $\theta = 2.5^\circ$. Beyond this twist-angle window, both Pfaffian and anti-Pfaffian ground state overlaps decrease, consistent with the emergence of an electron crystal. We remark that the finite-size clusters on used may frustrate crystal formation due to reduced rotation symmetry or incommensurability with a quadrupled unit cell, accounting for the non-zero model state overlap in the putative crystal regions. Our analysis shows that the non-Abelian FCI and crystal phases dominate the window of θ at hand.

Crystal in lowest-harmonic continuum model— Having established the broader phase diagram at $n = \frac{3}{2}$ in the adiabatic model, we now turn to the lowest-harmonic continuum model for tMoTe₂ [1]. We focus on angles $\theta > 1.9^\circ$ where the first two non-interacting minibands both have $C = +1$ given the parameters of Ref. [11]. In Fig. 3(a), we show the many-body energy spectrum at $n = \frac{3}{2}$ and $\theta = 2.6^\circ$, where the four lowest energy levels are isolated and nearly degenerate. Their center-of-mass

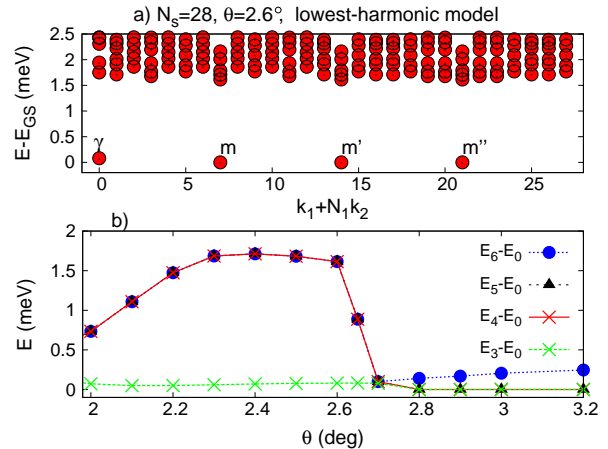


FIG. 3. **Electron crystal phase from the lowest-harmonic tMoTe₂ model** (a) Energy spectrum at half filling of the second moiré miniband for $\theta = 2.6^\circ$. (b) Excitation gaps versus twist angle θ . We use $\epsilon = 5$ and cluster 28 [34].

crystal momenta differ by m -point wavevectors, consistent with 2×2 symmetry breaking. Fig. 3 (b) shows that this property holds over a wide range of twist angles $2.0^\circ \leq \theta \leq 2.65^\circ$. As in the adiabatic model, we find that signatures of crystallization in density correlation functions are suppressed [34]. When $\theta > 2.65^\circ$, the 4-fold ground state degeneracy disappears. Instead, we find 6 ground states at low-symmetry momenta, consistent with a Landau Fermi liquid.

Topology and anti-topology of the crystals— We now study the quantized Hall response $\sigma_H = C \frac{e^2}{h}$ of the incompressible electron crystals by calculating their many-body Chern numbers [38]. Within our calculation scheme, the total Chern number of the many-body state $C_{tot} = C_1 + C_2$ is the sum of the Chern number C_1 of the full first band and the Chern number of the many-body state in the partially occupied second band C_2 .

First, we address the adiabatic model. As shown in Fig. 4 (a), we find $C_2 = \frac{1}{2}$ at $\theta = 2.6^\circ$ and therefore $C_{tot} = \frac{3}{2}$ as expected for a Pfaffian fractional Chern insulator. For $1.8^\circ \lesssim \theta \lesssim 2^\circ$, we find $C_2 = -1$. However, for $2^\circ \lesssim \theta \lesssim 2.4^\circ$ we find $C_2 = +1$ and for $2.7^\circ \lesssim \theta$, we find $C_2 = 0$. Our calculations indicate the existence of three distinct crystals with the same 2×2 enlarged unit cell but different Chern numbers $C_{tot} = 0, 2,$ and 1 .

We now turn to the crystal in the lowest-harmonic model. As shown in Fig. 4(b), we find $C_2 = -1$, for each of the four quasidegenerate ground states in the window $2.0^\circ \leq \theta \leq 2.65^\circ$. The system is, therefore, an anti-topological crystal with $C_{tot} = 0$. In the metallic phase at $\theta > 2.65^\circ$, the finite-size Chern number differs between the lowest-energy states at γ and m and are not meaningful in the thermodynamic limit.

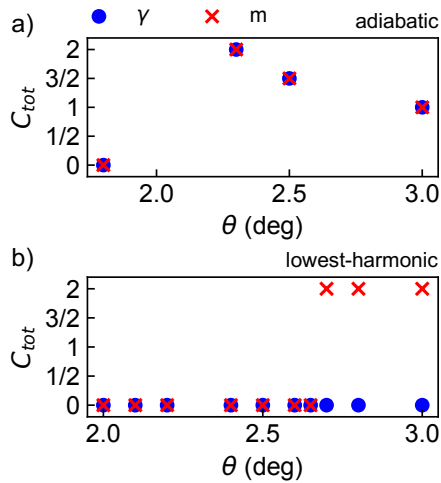


FIG. 4. **Many-body Chern number.** Total many-body Chern number, $C_{tot} = C_1 + C_2$ (see text) in (a) the adiabatic model and (b) lowest-harmonic model at several representative twist angles. $n = \frac{3}{2}$ and full spin polarization is assumed. We use $\epsilon = 5$ and cluster 28 [34].

Hartree-Fock study of anti-topological crystal— To complement our exact diagonalization results, we perform a self-consistent unrestricted Hartree-Fock (HF) study at $n = \frac{3}{2}$ in the lowest-harmonic continuum model of $t\text{MoTe}_2$. We assume full spin/valley polarization and allow for spontaneous quadrupling of the moiré unit cell. Unlike in our ED study, here we work in a plane-wave basis and do not project to any subset of moiré bands. Figs 5(a) and 5(b) show the hole density $n(\mathbf{r})$ and HF band structure of the self-consistent ground state respectively. The hole density has a 2×2 enlarged unit cell relative to the moiré superlattice. Additionally, the band structure has a gap at the Fermi level as a consequence of spontaneous discrete translation symmetry breaking. $n = \frac{3}{2}$ of a hole per moiré unit cell equates to 6 holes per symmetry-broken unit cell and thus 6 occupied HF bands. The first 4 occupied HF bands originate from the first non-interacting band and thus carry a cumulative Chern number of +1. The 5th and 6th occupied HF bands originate from the second non-interacting band and carry Chern numbers of 0 and -1 respectively. Therefore, the self-consistent HF ground state is an anti-topological crystal with a 2×2 enlarged unit cell and $C_{tot} = 0$, in agreement with our ED study. This demonstrates that the anti-topological crystal is robust against band mixing effects.

Crucially, the anti-topological crystal is robust to band inversions which modify the non-interacting Chern number of the partially filled band. Fig. 5(d) shows that the gap $\Delta_{6,7}$ between the highest occupied (6th) and lowest unoccupied (7th) HF bands remains open from $\theta = 2.6^\circ$ to 3° , while the gap between the eighth and ninth symmetry-broken subbands $\Delta_{8,9}$ closes at $\theta \approx$

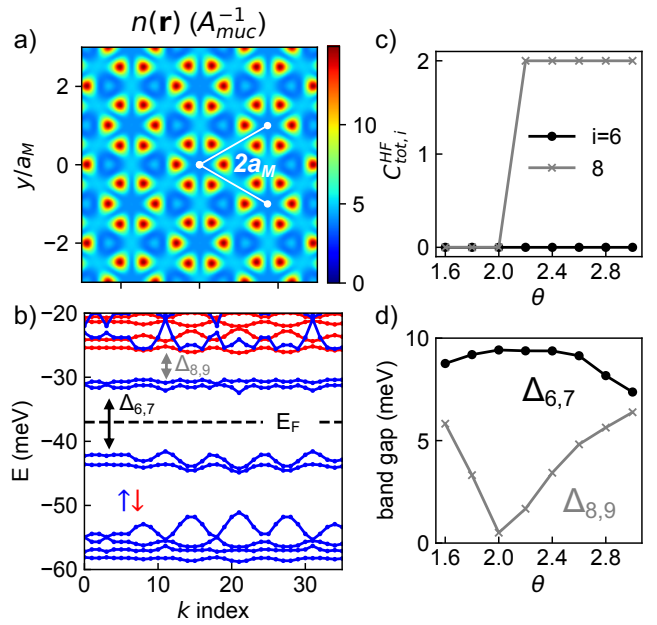


FIG. 5. **Anti-topological crystal in the Hartree-Fock approximation.** (a) Hole density $n(\mathbf{r})$ and (b) band structure (in the hole picture so the spectrum is bounded from below) of the HF ground state at $n = \frac{3}{2}$ and $\theta = 2.6^\circ$. Blue and red denote the occupied and unoccupied spin/valley respectively. The k index labels crystal momenta in quadrupled unit cell [34]. (c) Cumulative Chern number, $C_{tot,i}^{HF} = \sum_{j=1}^i C_j^{HF}$ where C_j^{HF} is the Chern number of the j^{th} symmetry-broken subband, as a function of twist angle. $C_{tot,6}^{HF}$ is the Chern number of the HF ground state at $n = \frac{3}{2}$ and $C_{tot,8}^{HF}$ is the total Chern number of the set of subbands corresponding to the lowest two symmetry-unbroken moiré bands. (d) Minimum direct bandgap between the highest-occupied and lowest-unoccupied subbands $\Delta_{6,7}$, as well as the gap corresponding to that between the second and third symmetry-unbroken moiré bands, $\Delta_{8,9}$. Full spin polarization is assumed. $\epsilon = 20$ and cluster 144 are used.

2.0° . Moreover, Fig. 5(c) shows that the cumulative Chern number of the 8 lowest symmetry-broken subbands changes from 0 to 2 at this gap closing. This reflects an inversion between the second and third non-interacting moiré bands at a nearby twist angle of $\theta \approx 1.9^\circ$ during which the total Chern number of the lowest two non-interacting bands changes from 0 to 2. Therefore, the HF ground states on either side of the non-interacting band inversion are both crystals with $C_{tot} = 0$ and are adiabatically connected.

Discussion— In this work, we have studied novel electron crystals emerging at half-filling of the second mini-band in twisted MoTe_2 . These crystals appear near in twist angle to a non-Abelian FCI state in the adiabatic model. While they share a common translation symmetry-breaking pattern of a 2×2 -enlarged unit cell, they differ in their quantized Hall responses. In the adiabatic model, we find $\sigma_H = 0$, $2\frac{e^2}{h}$, and $\frac{e^2}{h}$ in three differ-

ent cases which are all distinct from the competing non-Abelian FCI which exhibits $\sigma_H = \frac{3}{2} \frac{e^2}{h}$. In the lowest-harmonic model, we find a single crystal with $\sigma_H = 0$. This crystal occurs at half-filling of the second miniband over a range of angles, including some where then first two non-interacting moiré bands have the same Chern number of +1. In this case, the vanishing of the Hall conductance occurs due to cancellation between contributions from the parts of the many-body state in the full first band (+1) and the half-full second band (-1). For this reason, we call it an *anti-topological* crystal.

The anti-topological crystal is distinct from electron crystals in partially occupied Chern bands studied previously. For example, the anti-topological crystal differs from reentrant integer quantum Hall states in which a crystal forms on top of an integer quantum Hall vacuum. The Chern number of the many-body wavefunction projected to the second miniband is *opposite* to the band Chern number itself. In this respect, it differs from conventional quantum Hall states and previously studied quantum anomalous Hall crystals [32].

Moreover, the anti-topological crystal exists at a half-integer filling factor and has two electrons per symmetry-broken unit cell (in addition to four coming from the full first band). In these ways, it differs from a Wigner crystal near an integer filling factor with one particle per symmetry-broken unit cell. While the anti-topological crystal is topologically trivial, it should exist in proximity to topological states such as a $C = 2$ Chern insulator at $n = 2$. This contrasts a scenario in which the topological character of the underlying moiré bands is nullified by interaction effects at higher filling factors.

Acknowledgments.— We thank Xiaodong Xu for insightful discussions. The work at Massachusetts Institute of Technology was supported by the Air Force Office of Scientific Research (AFOSR) under Award No. FA9550-22-1-0432 and benefited from computing resources provided by the MIT SuperCloud and Lincoln Laboratory Supercomputing Center. A.P.R. was supported in part by grant NSF PHY-2309135 to the Kavli Institute for Theoretical Physics (KITP). D.N.S. was supported by the U.S. Department of Energy, Office of Basic Energy Sciences under Grant No. DE-FG02-06ER46305. A.A. was supported by the Knut and Alice Wallenberg Foundation (KAW 2022.0348). E.J.B. was supported by the Swedish Research Council (2018-00313 and 2024-04567), the Knut and Alice Wallenberg Foundation (2018.0460 and 2023.0256) and the Göran Gustafsson Foundation for Research in Natural Sciences and Medicine. L. F. was partly supported by the Simons Investigator Award from the Simons Foundation.

* areddy@mit.edu

- † donna.sheng1@csun.edu
 ‡ ahmed95@mit.edu
 § emil.bergholtz@fysik.su.se
 ¶ liangfu@mit.edu
- [1] F. Wu, T. Lovorn, E. Tutuc, I. Martin, and A. MacDonald, Topological insulators in twisted transition metal dichalcogenide homobilayers, *Physical review letters* **122**, 086402 (2019).
 - [2] T. Devakul, V. Crépel, Y. Zhang, and L. Fu, Magic in twisted transition metal dichalcogenide bilayers, *Nature communications* **12**, 6730 (2021).
 - [3] V. Crépel and L. Fu, Anomalous hall metal and fractional chern insulator in twisted transition metal dichalcogenides, *Physical Review B* **107**, L201109 (2023).
 - [4] E. Anderson, F.-R. Fan, J. Cai, W. Holtzmann, T. Taniguchi, K. Watanabe, D. Xiao, W. Yao, and X. Xu, Programming correlated magnetic states with gate-controlled moiré geometry, *Science* **381**, 325 (2023).
 - [5] J. Cai, E. Anderson, C. Wang, X. Zhang, X. Liu, W. Holtzmann, Y. Zhang, F. Fan, T. Taniguchi, K. Watanabe, *et al.*, Signatures of fractional quantum anomalous hall states in twisted mote₂, *Nature* **622**, 63 (2023).
 - [6] B. A. Foutty, C. R. Kometter, T. Devakul, A. P. Reddy, K. Watanabe, T. Taniguchi, L. Fu, and B. E. Feldman, Mapping twist-tuned multiband topology in bilayer wse₂, *Science* **384**, 343 (2024).
 - [7] Y. Zeng, Z. Xia, K. Kang, J. Zhu, P. Knüppel, C. Vaswani, K. Watanabe, T. Taniguchi, K. F. Mak, and J. Shan, Thermodynamic evidence of fractional chern insulator in moiré mote₂, *Nature* **622**, 69 (2023).
 - [8] F. Xu, Z. Sun, T. Jia, C. Liu, C. Xu, C. Li, Y. Gu, K. Watanabe, T. Taniguchi, B. Tong, *et al.*, Observation of integer and fractional quantum anomalous hall effects in twisted bilayer mote₂, *Physical Review X* **13**, 031037 (2023).
 - [9] H. Park, J. Cai, E. Anderson, Y. Zhang, J. Zhu, X. Liu, C. Wang, W. Holtzmann, C. Hu, Z. Liu, *et al.*, Observation of fractionally quantized anomalous hall effect, *Nature* **622**, 74 (2023).
 - [10] H. Li, U. Kumar, K. Sun, and S.-Z. Lin, Spontaneous fractional chern insulators in transition metal dichalcogenide moiré superlattices, *Physical Review Research* **3**, L032070 (2021).
 - [11] A. P. Reddy, F. Alsallom, Y. Zhang, T. Devakul, and L. Fu, Fractional quantum anomalous hall states in twisted bilayer mote₂ and wse₂, *Phys. Rev. B* **108**, 085117 (2023).
 - [12] C. Wang, X.-W. Zhang, X. Liu, Y. He, X. Xu, Y. Ran, T. Cao, and D. Xiao, Fractional chern insulator in twisted bilayer mote₂, *Physical Review Letters* **132**, 036501 (2024).
 - [13] H. Goldman, A. P. Reddy, N. Paul, and L. Fu, Zero-field composite fermi liquid in twisted semiconductor bilayers, *Physical Review Letters* **131**, 136501 (2023).
 - [14] J. Dong, J. Wang, P. J. Ledwith, A. Vishwanath, and D. E. Parker, Composite fermi liquid at zero magnetic field in twisted mote₂, *Physical Review Letters* **131**, 136502 (2023).
 - [15] A. P. Reddy and L. Fu, Toward a global phase diagram of the fractional quantum anomalous hall effect, *Physical Review B* **108**, 245159 (2023).
 - [16] K. Kang, B. Shen, Y. Qiu, Y. Zeng, Z. Xia, K. Watanabe, T. Taniguchi, J. Shan, and K. F. Mak, Evidence of

- the fractional quantum spin hall effect in moiré mote₂, *Nature* **628**, 522 (2024).
- [17] L. Wang, E.-M. Shih, A. Ghiotto, L. Xian, D. A. Rhodes, C. Tan, M. Claassen, D. M. Kennes, Y. Bai, B. Kim, *et al.*, Correlated electronic phases in twisted bilayer transition metal dichalcogenides, *Nature materials* **19**, 861 (2020).
- [18] A. P. Reddy, N. Paul, A. Abouelkomsan, and L. Fu, Non-abelian fractionalization in topological minibands, *Phys. Rev. Lett.* **133**, 166503 (2024).
- [19] C. Xu, N. Mao, T. Zeng, and Y. Zhang, Multiple chern bands in twisted mote₂ and possible non-abelian states (2024), [arXiv:2403.17003](https://arxiv.org/abs/2403.17003).
- [20] F. Chen, W.-W. Luo, W. Zhu, and D. Sheng, Robust non-abelian even-denominator fractional chern insulator in twisted bilayer mote₂, *arXiv preprint arXiv:2405.08386* (2024).
- [21] C. Wang, X.-W. Zhang, X. Liu, J. Wang, T. Cao, and D. Xiao, Higher landau-level analogues and signatures of non-abelian states in twisted bilayer mote₂, *arXiv preprint arXiv:2404.05697* (2024).
- [22] C.-E. Ahn, W. Lee, K. Yananose, Y. Kim, and G. Y. Cho, Non-abelian fractional quantum anomalous hall states and first landau level physics of the second moiré band of twisted bilayer mote₂, *Physical Review B* **110**, L161109 (2024).
- [23] R. Willett, J. P. Eisenstein, H. L. Störmer, D. C. Tsui, A. C. Gossard, and J. H. English, Observation of an even-denominator quantum number in the fractional quantum Hall effect, *Phys. Rev. Lett.* **59**, 1776 (1987).
- [24] G. Moore and N. Read, Nonabelions in the fractional quantum hall effect, *Nucl. Phys. B* **360**, 362 (1991).
- [25] M. Greiter, X.-G. Wen, and F. Wilczek, Paired hall state at half filling, *Physical review letters* **66**, 3205 (1991).
- [26] R. H. Morf, Transition from quantum hall to compressible states in the second landau level: new light on the $\nu=5/2$ enigma, *Physical review letters* **80**, 1505 (1998).
- [27] H. Liu, Z. Liu, and E. J. Bergholtz, Non-abelian fractional chern insulators and competing states in flat moiré bands, [arXiv preprint arXiv:2405.08887](https://arxiv.org/abs/2405.08887) (2024).
- [28] E. H. Rezayi and F. D. M. Haldane, Incompressible paired hall state, stripe order, and the composite fermion liquid phase in half-filled landau levels, *Physical Review Letters* **84**, 4685 (2000).
- [29] N. Morales-Durán, N. Wei, J. Shi, and A. H. MacDonald, Magic angles and fractional chern insulators in twisted homobilayer transition metal dichalcogenides, *Phys. Rev. Lett.* **132**, 096602 (2024).
- [30] D. Zhai and W. Yao, Theory of tunable flux lattices in the homobilayer moiré of twisted and uniformly strained transition metal dichalcogenides, *Physical Review Materials* **4**, 094002 (2020).
- [31] J. Shi, N. Morales-Durán, E. Khalaf, and A. MacDonald, Adiabatic approximation and aharonov-casher bands in twisted homobilayer transition metal dichalcogenides, *Physical Review B* **110**, 035130 (2024).
- [32] D. Sheng, A. P. Reddy, A. Abouelkomsan, E. J. Bergholtz, and L. Fu, Quantum anomalous hall crystal at fractional filling of moiré superlattices, *Physical Review Letters* **133**, 066601 (2024).
- [33] H. Park, J. Cai, E. Anderson, X.-W. Zhang, X. Liu, W. Holtzmann, W. Li, C. Wang, C. Hu, Y. Zhao, *et al.*, Ferromagnetism and topology of the higher flat band in a fractional chern insulator, *arXiv preprint arXiv:2406.09591* (2024).
- [34] See the Supplemental Material.
- [35] N. Read and D. Green, Paired states of fermions in two dimensions with breaking of parity and time-reversal symmetries and the fractional quantum Hall effect, *Phys. Rev. B* **61**, 10267 (2000).
- [36] E. Rezayi, F. Haldane, and K. Yang, Charge-density-wave ordering in half-filled high landau levels, *Physical review letters* **83**, 1219 (1999).
- [37] F. Haldane, E. Rezayi, and K. Yang, Spontaneous breakdown of translational symmetry in quantum hall systems: Crystalline order in high landau levels, *Physical review letters* **85**, 5396 (2000).
- [38] D. Sheng, Z.-C. Gu, K. Sun, and L. Sheng, Fractional quantum hall effect in the absence of landau levels, *Nature communications* **2**, 389 (2011).

Supplemental Material for *Anti-topological crystal and non-Abelian liquid in twisted semiconductor bilayers*

CONTENTS

I. Projected structure factor	1
II. Many-body Berry curvature	2
III. Miscellaneous	4
References	4

I. PROJECTED STRUCTURE FACTOR

As mentioned in the main text, the 1LL-like character of the second miniband’s wavefunctions suppresses finite-size Bragg peaks. In Fig. 1, we show the projected structure factor $s(\mathbf{q})$ of the adiabatic model’s ground state at several twist angles. In contrast to the modified structure factor $\tilde{s}(\mathbf{q})$ shown in Fig. 1 of the main text, $s(\mathbf{q})$ does not show incipient Bragg peaks at $\theta = 3^\circ$. Moreover, unlike $\tilde{s}(\mathbf{q})$, $s(\mathbf{q})$ does not contrast sharply between $\theta = 2.5^\circ$ and 3° . At $\theta = 2^\circ$, $s(\mathbf{q})$ shows Bragg peaks at moiré reciprocal lattice vectors (*not* the reciprocal lattice vectors of the quadrupled unit cell, which are the m points of the moiré Brillouin zone). This reflects the more localized character of the second miniband’s wavefunctions at smaller angles. We note that the ordinary structure factor $S(\mathbf{q}) = \frac{1}{N} \langle \rho(-\mathbf{q}) \rho(\mathbf{q}) \rangle$ (not shown) also does not show clear signatures of crystallization.

The origin of this behavior is as follows. The density operator projected to the nLL is $\bar{\rho}_n(\mathbf{q}) = P_{\text{nLL}} \rho(\mathbf{q}) P_{\text{nLL}} = P_{\text{nLL}} \sum_i e^{i\mathbf{q}\cdot\mathbf{r}_i} P_{\text{nLL}} = L_n(\frac{\ell^2 q^2}{2}) \tau_i(\mathbf{q}) P_{\text{nLL}}$ where $\tau_i(\mathbf{q})$ is a LL-index-independent magnetic translation operator acting on particle i (see, for instance, the Supplemental Material of Ref. [1]). Formally, one can map a many-body state in a given Landau level to any other Landau level by acting with a product of Landau level index ladder operators. Under this mapping, the projected structure factor of the state in the nLL is related to that of the state in the LLL as $s_{\text{nLL}}(\mathbf{q}) = \frac{1}{N} \langle \bar{\rho}_n(-\mathbf{q}) \bar{\rho}_n(\mathbf{q}) \rangle = \left[L_n(\frac{\ell^2 q^2}{2}) \right]^2 s_{\text{LLL}}(\mathbf{q})$ where $L_n(x)$ is a Laguerre polynomial. Now $L_1(\frac{\ell^2 q^2}{2} = 1) = 0$, which implies that $s_{\text{1LL}}(q_0 \equiv \frac{\sqrt{2}}{\ell}) = 0$. Within the adiabatic model, the effective magnetic length ℓ and moiré lattice

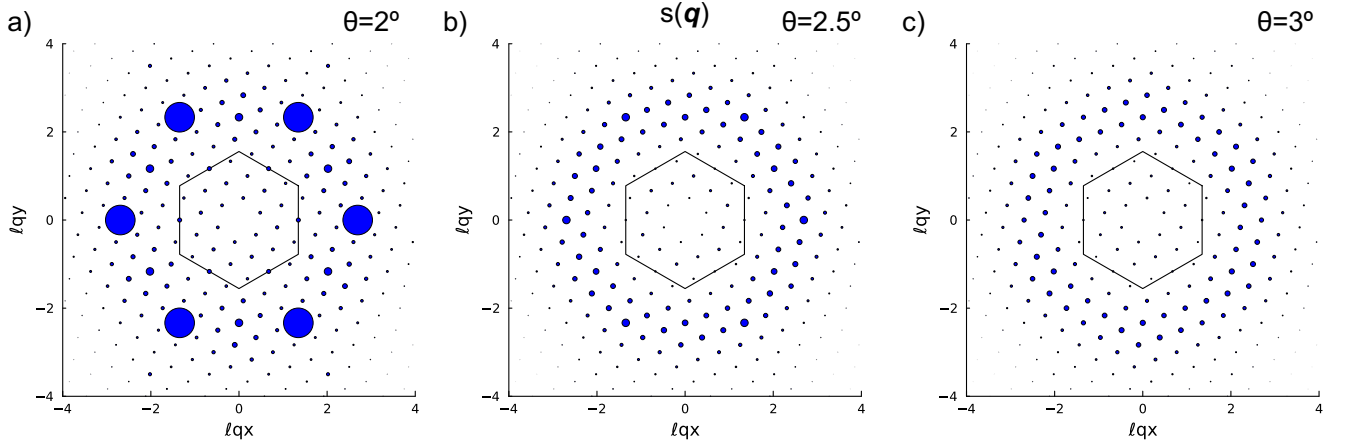


FIG. 1. Projected structure factor $s(\mathbf{q}) = \frac{1}{N} \langle \bar{\rho}_2(-\mathbf{q}) \bar{\rho}_2(\mathbf{q}) \rangle$ of the ground state at $n = \frac{3}{2}$ in the adiabatic model. Here $\langle \hat{O} \rangle = \frac{1}{N_{GS}} \sum_{i \in GS} \langle \Psi_i | \hat{O} | \Psi_i \rangle$ is an average over exactly degenerate ground states. Here $\bar{\rho}_2(\mathbf{q}) = \sum_{\mathbf{k}} \langle u_{2, \mathbf{k}-\mathbf{q}} | u_{\mathbf{k}} \rangle c_{2, \mathbf{k}-\mathbf{q}}^\dagger c_{2, \mathbf{k}}$ is the projected density operator of the second miniband. Compare to the “modified” structure factor defined in the main text and shown in Fig. 1.

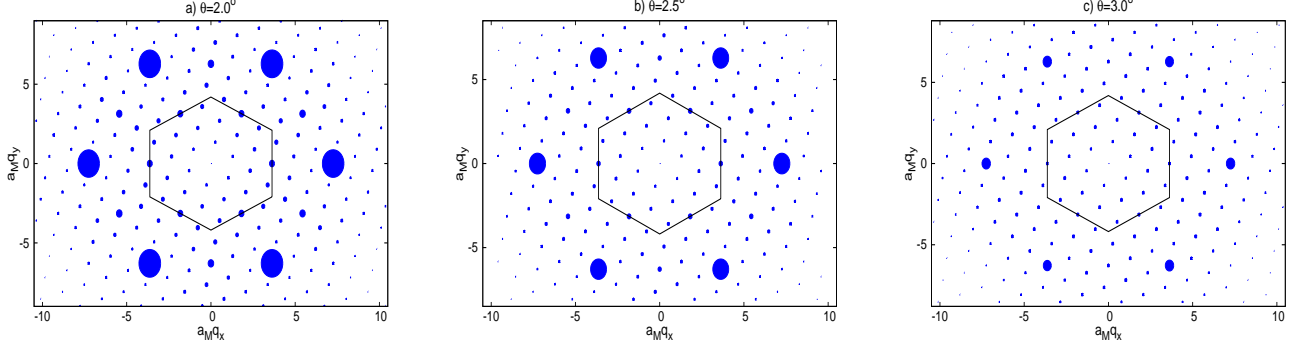


FIG. 2. Projected structure factor $s(\mathbf{q}) = \frac{1}{N} \langle \bar{\rho}_2(-\mathbf{q}) \bar{\rho}_2(\mathbf{q}) \rangle$ of the ground state at $n = \frac{3}{2}$ in the lowest-harmonic model. Here $\bar{\rho}_2(\mathbf{q})$ is the projected density operator of the second miniband.

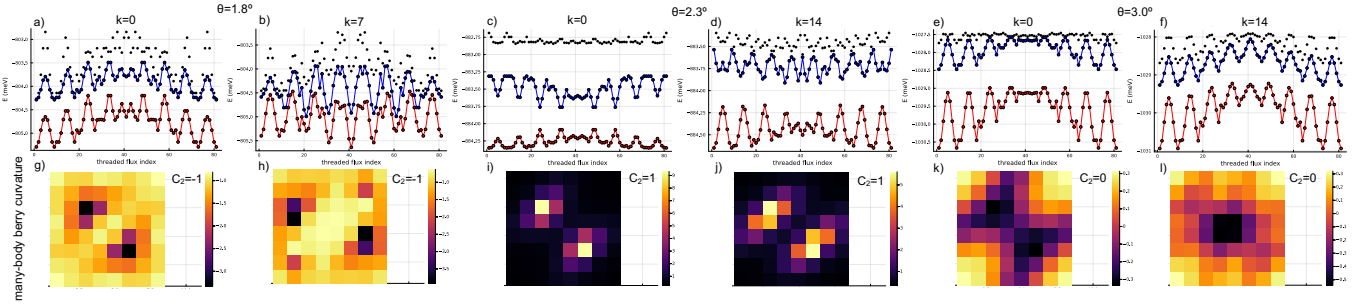


FIG. 3. Many-body Berry curvature and Chern number at representative twist angles of the three distinct electronic crystals in the adiabatic model. $\epsilon = 5$. Cluster 28 is used. In (a-f), the three lowest energy levels with a given center-of-mass momentum quantum number k are shown. The lowest is highlighted in red and the second lowest in blue, with lines added to guide the eye. The many-body Berry curvature is in units such that its average is C_2 .

constant a_M are related by the property that the moiré unit cell encloses one effective flux quantum: $2\pi\ell^2 = \frac{\sqrt{3}}{2}a_M^2$. The magnitude of the m point wavevectors is then $|m| = \frac{2\pi}{\sqrt{3}} \frac{1}{a_M} = \sqrt{\frac{\pi}{3}} \frac{1}{\ell} \approx 0.95q_0$. Therefore, when the second band is 1LL-like, suppression of finite size Bragg peaks at the m points is expected because $q = |m|$ is very close to a zero in $L_1(\frac{\ell^2 q^2}{2})$. Specifically, $[L_1(\frac{\ell^2 q^2}{2})]^2 = s_{1LL}(|m|)/s_{LLL}(|m|) \approx 0.009$. Finally, Ref. [1] shows that the second miniband in the adiabatic model is indeed 1LL-like in a precise way, confirming the relevance of our LL-based argument to the adiabatic model.

In comparison, in Fig. 2, we show the projected structure factor $s(\mathbf{q})$ of the lowest-harmonic model's ground state at several twist angles. At $\theta = 2^\circ$, $s(\mathbf{q})$ shows Bragg peaks at moiré reciprocal lattice vectors similar to the results of the adiabatic model. For the lowest-harmonic model, the $s(\mathbf{q})$ varies less with twist angles with no sharp peaks within the moiré Brillouin zone.

II. MANY-BODY BERRY CURVATURE

We define the many-body Chern number as

$$C = 2\pi i \int_0^1 d\phi_1 \int_0^1 d\phi_2 \left[\left\langle \frac{\partial \Psi}{\partial \phi_1} \middle| \frac{\partial \Psi}{\partial \phi_2} \right\rangle - \left\langle \frac{\partial \Psi}{\partial \phi_2} \middle| \frac{\partial \Psi}{\partial \phi_1} \right\rangle \right]. \quad (1)$$

Here $|\Psi(\phi)\rangle$ is a many-body eigenstate of $H(\phi) = U(\phi) H U^\dagger(\phi)$ where $U(\phi) = e^{i(\phi_1 \mathbf{T}_1 + \phi_2 \mathbf{T}_2) \cdot \sum_i \mathbf{r}_i}$. $\mathbf{L}_{1/2}$ are the primitive boundary vectors of the torus and $\mathbf{T}_a = \frac{2\pi \epsilon_{ab} \mathbf{L}_b \times \hat{z}}{|\mathbf{L}_1 \times \mathbf{L}_2|}$ are the primitive wavevectors.

Here we show the many-body Berry curvature and Chern numbers computed for degenerate or quasidegenerate ground states at various twist angles, elaborating on the results shown in Fig. 4 of the main text. In practice, we

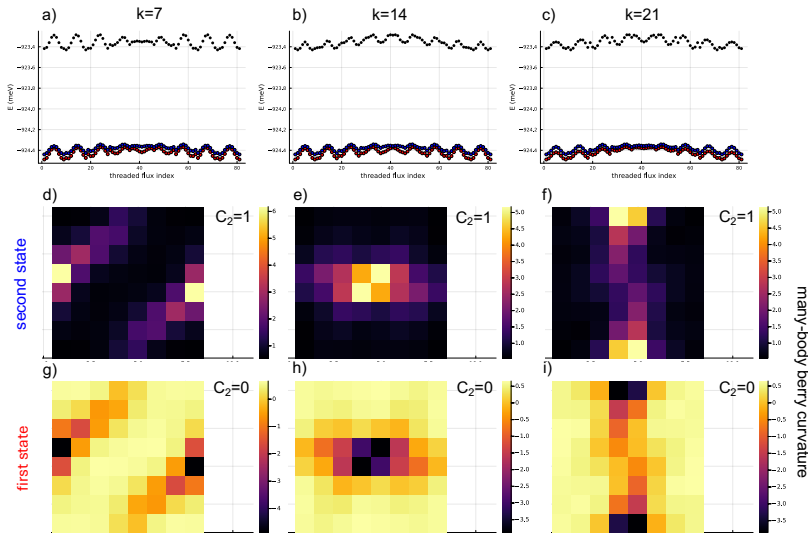


FIG. 4. Analogous to Fig. 3 but for the fractional Chern insulator state at $\theta = 2.5^\circ$ in the adiabatic model. $\epsilon = 5$ and cluster 28 is used.

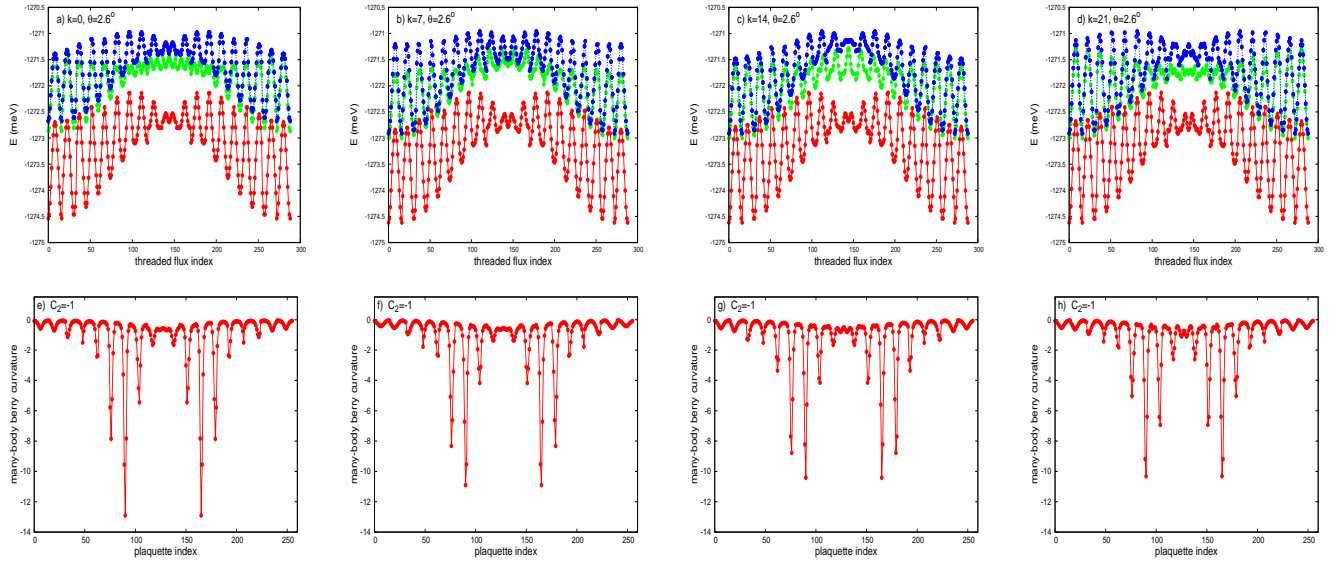


FIG. 5. Energy spectrum, many-body Berry curvature and Chern number at $\theta = 2.6$ and $\epsilon = 5$ in the lowest-harmonic model. Cluster 28 is used. In (a-d), the three lowest energy levels with a given center-of-mass momentum quantum number k are shown. The lowest is highlighted in red, the second lowest in green and the third lowest in blue, with lines added to guide the eye. The many-body Berry curvature is in units such that its average is C .

approximate the Berry curvature and Chern number by computing the discrete Berry flux through each plaquette of a discrete grid of threaded flux values (ϕ_i in Eq. 1) following the method described in Ref. [2]. This discrete method are generally reliable when the computed Berry flux through each plaquette, in units such that its average is the Chern number C , is much less than the number of plaquettes and varies smoothly between neighboring plaquettes. Specifically, we show C_2 , the contribution to the total Chern number $C_{tot} = C_1 + C_2$ coming from the half-filled second band and its associated Berry flux. $C_1 = 1$ is the contribution from the full first band.

Fig. 3 shows data for the crystals and Fig. 4 shows data for the fractional Chern insulator. For each of the crystals, there is one ground state at each of the symmetry-related but inequivalent m points ($k = 7, 14, 21$ on cluster 28) and one at the γ point ($k = 0$ on cluster 28). We show data for the γ point ground state and for one representative of the three symmetry-related m points. In each case, the four quasidegenerate ground states have the same Chern number.

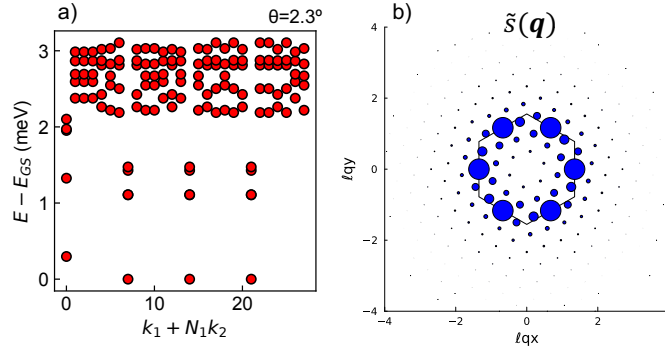


FIG. 6. (a) Many-body spectrum and (b) modified structure factor at $\theta = 2.3^\circ$ in the adiabatic model. $\epsilon = 5$ and cluster 28 are used.

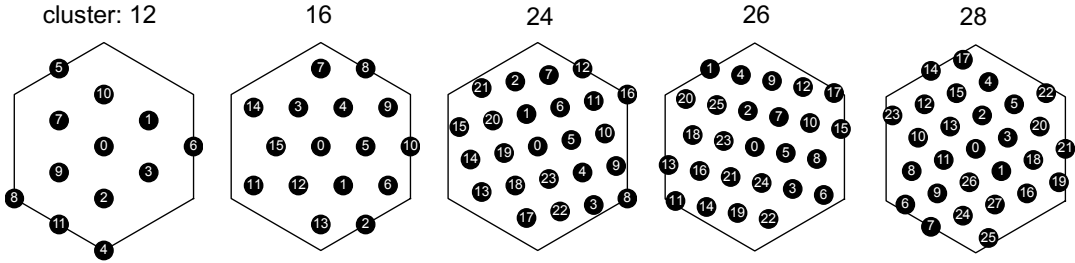


FIG. 7. Momentum-space diagrams of finite-size clusters used in our exact diagonalization calculations. Each momentum point is labeled by an index $k = k_1 + N_1 k_2$.

For the fractional Chern insulator, there are two degenerate ground states at each of the three inequivalent m points. At each m point, the Chern number of the lowest state is 0 and the Chern number of the second state is 1, as shown in Fig. 4. Therefore, the average Chern number of the sixfold degenerate ground state manifold is $C_2 = \frac{1}{2}$ as expected for a Pfaffian-like fractional Chern insulator.

We also show data for the crystal phase of the lowest-harmonic model Fig. 5. There is one ground state at each of the symmetry-related but inequivalent m points ($k = 7, 14, 21$ on cluster 28) and one at the γ point ($k = 0$ on cluster 28). We show data for these ground states at $\theta = 2.6$ and $\epsilon = 5$. In each case, the four quasidegenerate ground states have the same Chern number $C_2 = -1$ (we set the band Chern number as the reference $C_1 = 1$ and C_2 has the opposite sign to C_1 with $C_1 + C_2 = 0$).

III. MISCELLANEOUS

Fig. 6 shows an example many-body spectrum and modified structure factor at $\theta = 2.3^\circ$ in the adiabatic model.

Fig. 7 shows momentum-space diagrams of the finite-size clusters we use for exact diagonalization calculations in this work.

In Fig. 5(b) of the main text, the crystal momentum wavevector $\mathbf{k} = k_1 \mathbf{T}'_1 + k_2 \mathbf{T}'_2$ is assigned the k index $k_1 + N_1 k_2$ where $\mathbf{T}'_i = \mathbf{b}'_i / N_i$ and $N_1 = N_2 = 36$. $\mathbf{b}'_1 = \frac{2\pi}{\sqrt{3}a_M}(1, 0)$ and $\mathbf{b}'_2 = \frac{2\pi}{\sqrt{3}a_M}(-\frac{1}{2}, \frac{\sqrt{3}}{2})$ are primitive reciprocal lattice vectors of the quadrupled moiré unit cell.

-
- [1] A. P. Reddy, N. Paul, A. Abouelkomsan, and L. Fu, *Phys. Rev. Lett.* **133**, 166503 (2024).
 [2] T. Fukui, Y. Hatsugai, and H. Suzuki, *Journal of the Physical Society of Japan* **74**, 1674 (2005).